

## ORIGINAL RESEARCH PAPER

# Newly designed identifying method for ice thickness on high-voltage transmission lines via machine vision

Bingjun Weng<sup>1</sup> | Wei Gao<sup>1</sup> | Weicou Zheng<sup>2</sup> | Gengjie Yang<sup>1</sup>

<sup>1</sup>College of Electrical Engineering and Automation, Fuzhou University, Fuzhou, Fujian, China

<sup>2</sup>Ningde Power Supply Company of State Grid Fujian Electric Power Co., Ltd, Ningde, Fujian, China

## Correspondence

Wei Gao, College of Electrical Engineering and Automation, Fuzhou University, Fuzhou, Fujian 350108, China.

Email: gaowei0203@fzu.edu.cn

Associate Editor: Shahab Farokhi

## Funding information

National Natural Science Foundation of China, Grant/Award Number: 51677030

## Abstract

The icing of transmission lines will bring considerable challenges to the safe operation of the power grid. Therefore, a novel method combines machine vision and machine learning algorithms for identifying the ice thickness on high-voltage transmission line (HVTL) as proposed herein. First, noise and background interference in the image are filtered, and the grey image is used as input. Then, the algorithms of improved Canny edge detection, Hough transform, improved K-means clustering, and least-squares fitting are adopted in turn to locate the edges of conductors. Finally, according to the distance mapping model based on monocular vision, the ice thickness of the conductor is determined by calculating the width difference before and after icing. The experimental results show that the proposed method can accurately locate the edge of the conductor in both field and experimental environments. Moreover, it can ensure ideal effects under different illumination and hardly not be affected by distortion in both horizontal and vertical directions. Besides, the distance mapping model can map the pixel distance to the actual distance with high precision, no matter whether the background is simple or complex, and the calculated ice thickness has only a small deviation compared to the actual value. In addition, the proposed method shows high reliability and effectiveness when various interference such as different backgrounds, uneven icing, height difference changes, conductor movement, contrast changes, and conductor sag occur.

## 1 | INTRODUCTION

High-voltage transmission lines (HVTL) are prone to ice in the environment of low temperature, rain, and snow. Since icing will decrease the insulation performance, once the degree of icing exceeds the anti-icing capability of transmission lines, the insulation performance of power equipment will be significantly reduced, and accidents such as tripping and disconnection will occur. In extreme cases, the electric tower may even collapse, causing enormous economic losses [1–3]. In 2008, severe ice and snow disasters occurred in southern China. More than 36,000 transmission lines were damaged, a large number of electric towers collapsed, and continuous power failure occurred in many places, led to the power supply for more than 27 million households interrupted [4–6]. Nowadays, abnormal weather phenomena occur frequently, and the hidden danger of ice coating on transmission lines in winter increases, so it must take more effective monitoring measures quickly.

In the early days, icing monitoring of the HVTL generally adopted manual observation by establishing ice observation stations. Operation and maintenance personnel simulated icing on transmission lines and insulators at ice observation stations near the transmission line and judged the degree of icing by long and short radius, weighing, etc. Manual observation can more intuitively reflect the icing status on-site, but with large error and insufficient timeliness. Simultaneously, due to the HVTL are often located on high mountains, operation and maintenance personnel have to go deep into areas with severe ice and snow disasters, which make them in danger [7, 8]. Fortunately, the system monitoring method of automatically measuring physical parameters through the monitoring terminal and transmitting them back to the monitoring centre master station via the communication network has become popular. It measures physical parameters such as line tension, dip, swing angle, and micro-meteorological parameters such as temperature, humidity, wind speed by sensors. Then in the background software of

This is an open access article under the terms of the Creative Commons Attribution-NonCommercial-NoDerivs License, which permits use and distribution in any medium, provided the original work is properly cited, the use is non-commercial and no modifications or adaptations are made.

© 2021 The Authors. *High Voltage* published by John Wiley & Sons Ltd on behalf of The Institution of Engineering and Technology and China Electric Power Research Institute.

the master station, the equivalent ice thickness is calculated combined with the mechanical model to determine the icing status [9–11]. Zhao et al. [12] developed an automatic icing warning system that calculated the thickness utilising stress measurement. Jiang et al. [13] introduced correction coefficients for wind load and uneven ice on the basis of traditional mechanical models. Thereby, a novel mechanical model for online icing monitoring of conductor was established. Ma et al. [14] used an optical load cell with a shearing structure and additional grooves to monitor ice coating, with no need for a power supply on-site and was immune to electromagnetic interference. The reliability and accuracy of the monitoring method based on mechanics are relatively high. However, the calculation process is quite complicated and easily affected by the environment. Moreover, sensors with high precision are absolutely necessary. Unfortunately, the structure of the transmission line has to be changed when the tension sensors and other devices are installed, so it can only be operated after a power failure, which affects the normal operation of the power grid and increases the operation and maintenance cost. In fact, public utilities need a simpler and more efficient way to realise ice observation.

With the development of machine vision technology, image processing methods have gradually become the mainstream of transmission line ice monitoring due to their powerful performance. Huang et al. [15] proposed an online ice detection technology using mechanical and visual sensors. In [15], the equivalent cross-sectional area of the conductor was obtained through the model established by the dual-camera pictures and the mechanical sensor, and the degree of icing was analysed after the shape of the iced conductor was restored by algorithms. However, large numbers of sensors are needed in [15], and the camera must be installed in a specific position, which makes it more difficult to apply on towers with limited space. Yang et al. [16] investigated a method of improved uniform local binary patterns (IULBP) to extract texture features of different ice types and identify iced insulators, but they did not further calculate the ice thickness. Guo et al. [17] adopted a method of binocular stereo vision combined with feature point matching based on a local multi-layer convolutional neural network to measure ice thickness. However, it has higher requirements for the installation position of the binocular camera, and the cameras on the tower are susceptible to shaking due to the strong wind, which affects the measurement accuracy. Guo et al. [18] and Ma et al. [19] all used unmanned aerial vehicles (UAV) equipped with binocular cameras to capture images of the transmission line to calculate the ice thickness automatically, but the climatic when icing was quite harsh, which affected the cruise of UAV. Li et al. [20] introduced an icing detection method based on machine vision, which utilising hardware calibration to find the relationship between the distance from the observation point to the object and the geometric size of each pixel in the image to calculate the ice thickness. However, in [20], the thickness is mapped by a simple linear model and has certain errors when calculating the actual width of conductor. Akram et al. [21] used images of the scanning electron microscope (SEM) to extract boundary conditions and then constructed a three-dimensional model of the target object

for analysis, but the modelling process of the algorithm is so complicated that makes it challenging to apply on HVTL. From the review of historical literature, it can be found that the machine vision algorithm is powerful and effective. The Canny operator uses a method of multi-stage detection to find edges of the image via gradient calculation. After non-maximum suppression and dual-threshold constraints, the edges are refined and filtered. It has the characteristics of high accuracy and fast speed, and is widely used in image edge extraction [22, 23]. But it is susceptible to noise and restricted to the complex background of the HVTL. The transmission line detection algorithm of Hough transform finds the straight lines that meets the conditions in the original space by accumulating the number of curves passing through a certain point in the parameter space, and it can accurately locate the transmission line in the image. It used to be applied to identify the lane line of unmanned vehicles. In recent years, it has gradually been used in transmission line identification [24]. However, the transmission line detection of Hough transform requires other algorithms to obtain the image edge first, and the effect is not good when used alone. Zhao et al. [25] used the Ratio operator to detect the edges of transmission lines, and the edge images were analysed by four-connected region clustering to eliminate the noise. Then the Hough transform was adopted to extract the power lines. Finally, the line edges were obtained by the least-squares fitting. Hao et al. [26] introduced the 3-order B-spline function as the smooth function to construct wavelet bases to detect the icing image and then combined the Hough transform to connect the detected edges of the image to realise the identification of the icing transmission lines. Although the methods in [25, 26] have relatively good recognition results, they have too many steps, which reduce the calculation speed and leads to insufficient real-time performance. In addition to Canny detection and Hough transform, researchers are also exploring different schemes of transmission line recognition. For example, the method of scale-invariant feature transformation (SIFT) extracts edge points in an image by searching for key points in different scale spaces, and not interfered by illumination, affine transformation, and noise. Tian et al. [27] used SIFT to extract the static feature of the transmission line, and the experiments proved that the proposed method can still effectively match the corresponding feature points when the image was scaled or rotated, so as to identify the power equipment correctly. However, the background information of the HVTL image is abundant; it is hard for SIFT to determine whether the key points searched belong to the foreground or the background, which brings difficulties to the application. Moreover, compared with other electrical equipment such as insulators, the features of the transmission line are more concealed and difficult to identify. Even the improved feature point matching algorithms, such as speeded-up robust features (SURF) in [28] and Oriented Fast and Rotated Brief (ORB) in [29], both failed to solve this problem. In summary, it is challenging to identify the ice thickness of the transmission line only by a single algorithm, so it encourages this study to design a comprehensive algorithm to realise the target. To this end, an identification method for the ice thickness of HVTL based on dynamic slope

K-Means clustering and distance mapping is proposed by a series of research and experiments.

This study is organised into six chapters. Following the introduction, Chapter 2 briefly introduces the calculation process of the algorithm for ice thickness of the transmission line. Chapter 3 discusses the location method of transmission line with the emphasis on the improved K-Means clustering algorithm. The distance mapping method based on monocular vision is investigated in Chapter 4. In Chapter 5, the performance of the proposed method is analysed through experiments. Finally, the concluding remarks are given in Chapter 6.

## 2 | OVERVIEW OF THE PROPOSED METHOD

The proposed method in this study needs to identify and locate the conductor from the image, so as to fit the edge of the conductor and determine the actual ice-covering thickness according to the change of conductor width before and after icing. Specifically, it includes two steps, as shown in Figure 1.

- (i) *Conductors location*: The image of conductors should be pre-processed first, and then edge detection and line detection algorithms are combined to screen the straight-line segments of the edge of conductors. After that, each line segment is clustered to find their belonging. Finally, the line segments are fitted to determine the position of conductors.
- (ii) *Distance mapping and thickness calculation*: The internal parameters of the camera and environmental parameters are measured first, and then the actual width of the conductor is calculated through the distance mapping model. In the end, the ice thickness is equal to the difference of the conductor width before and after icing.

## 3 | CONDUCTORS LOCATION

### 3.1 | Image pre-processing

The image of HVTL often contains many background noises, which reduces the image quality and even submerges the features of the conductors. After analysis, it is found that Gaussian noise and impulse noise are the main ones. They should be removed by Gaussian filtering and median filtering, respectively, to ensure the accuracy of identification. In addition, morphological operations are used to remove black holes and white dots that cannot be filtered by the above two filtering algorithms. Since the captured colour image contains three channels of red, green and blue (RGB), the processing efficiency of the three channels separately is low, so the single-channel greyscale image is directly used as the research object. Figure 2 shows the comparison results before and after processing. There are trees and mountains in the original image (as shown in Figure 2a). The background is complex with serious noise interference, and the background features are even more significant than the features of conductors. After processing, the sharp features in the background (as shown in Figure 2b)



FIGURE 2 Image pre-processing (a) Original image, (b) Processed image

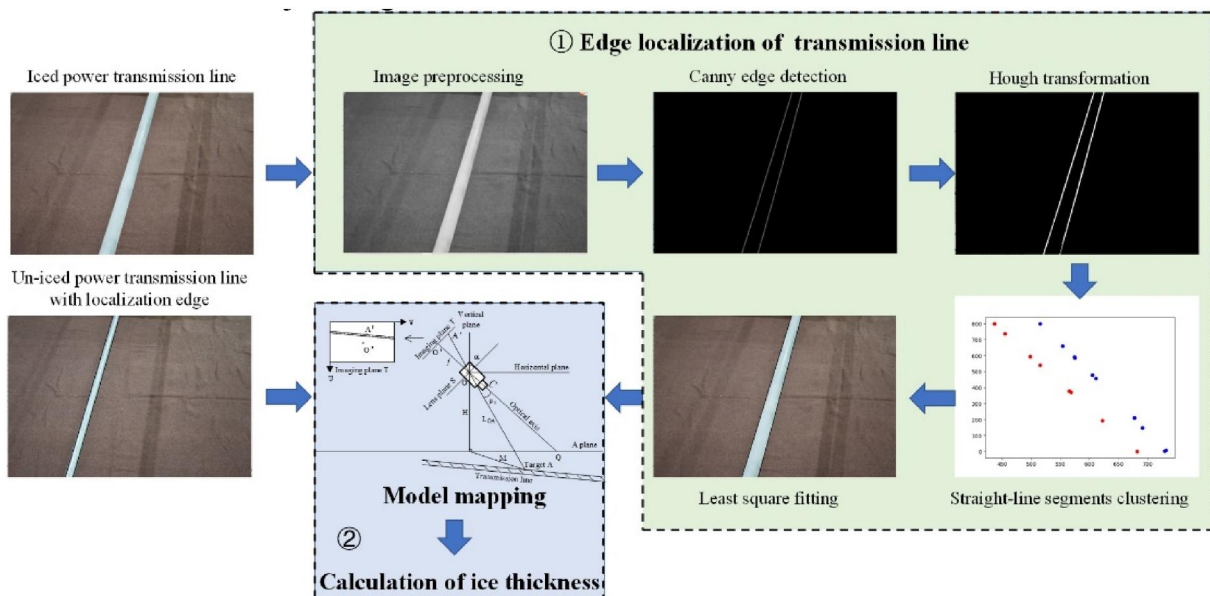


FIGURE 1 Recognition process of proposed method



are smoothed to make the features of conductors more prominent.

### 3.2 | Edge location of transmission line

The prerequisite for accurately identifying the icing condition of the conductor is to locate the edge of the conductor accurately. Therefore, an innovative algorithm of edge location is proposed, which includes four steps, namely edge detection, line detection, straight-line segments clustering, and edge fitting.

#### 3.2.1 | Edge detection

Before locating the edge of the conductor, all edges in the image should be extracted first. The Canny edge detection algorithm combined with the Sobel operator is usually the right choice [30]. However, this method focuses on detecting refined edges and ignores some weak edges with no prominent features. Unfortunately, the background environment of the HVTL corridor is complex, and the conductor features are easily submerged in the background interference and noise, and thus exist in the form of weak edges. Therefore, Scharr operator is used in this study to convolve the image, which enhances the performance of detecting the weak edges and ensures the integrity of the conductor edges. Figure 3 shows the comparison of the structure of the two operators in the horizontal direction. In the eight-connected region of testing points, the weights in Scharr operator are  $\pm 3$  and  $\pm 10$  instead of  $\pm 1$  and  $\pm 2$ . When convolving an image, the Scharr operator enhances the influence of points with smaller gradient values, so that weaker edge features are retained, and weak edges can be extracted. The operators in horizontal, vertical,  $+45^\circ$ ,  $-45^\circ$  directions convolve the greyscale image to obtain the corresponding gradient values  $G_x$ ,  $G_y$ ,  $G_{+45}$ , and  $G_{-45}$ .

After obtaining the gradient value, calculate the gradient amplitude and gradient angle in  $x$ - $y$  direction by formulas (1) and (2). The calculation for the  $\pm 45^\circ$  direction is similar.

$$G = \sqrt{G_x^2 + G_y^2} \quad (1)$$

$$\theta = \tan^{-1} \frac{G_y}{G_x} \quad (2)$$

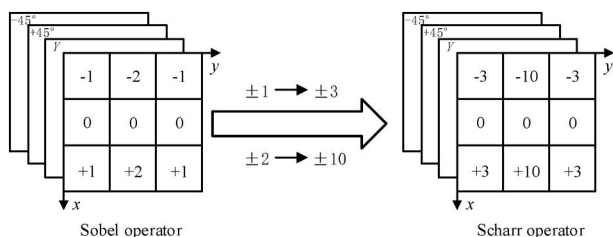


FIGURE 3 Comparison of Sobel and Scharr operator

At this time, the obtained edges are thick and contain multiple pixel widths. Firstly, it is necessary to refine them by the algorithm of non-maximum value suppression. Specifically, if the gradient value of a particular point is the largest in its local gradient direction, then it is retained, and vice versa. Then, the refined edges are selected by high and low thresholds. The points where the gradient amplitude is greater than the high threshold are strong edge points, those with a gradient less than the low threshold are non-edge points, and points between the two are weak edge points. Finally, the following rules are used to judge if it is an edge. All strong edge points are considered real edges, and if there is at least one strong edge point in the eight-connected region of a weak edge point, then the weak edge point is determined as a part of real edge. Otherwise, it is a non-edge point. After that, all edges in the image can be extracted.

Figure 4 shows the result of image convolution by Sobel operator and Scharr operator. The image convolved by the Sobel operator (as shown in Figure 4a-c) is more refined, with fine edges. While in the image convolved by the Scharr operator (as shown in Figure 4d-f), the edge information is more complicated, and the fineness of the edge is decreased, but it is more likely to find weaker edge information. Especially in Figure 4d, the feature of the conductor edge ignored by Sobel operator is completely extracted by Scharr operator. There are many background interferences in the HVTL image, and the gradient amplitude of the conductor edge may be smaller than that of the background interference. Therefore, the Sobel operator may erroneously extract the background edge information, resulting in missing conductor edges. Thus, it is meaningful to use the Scharr operator to extract more edges that are not obvious but may contain important information.

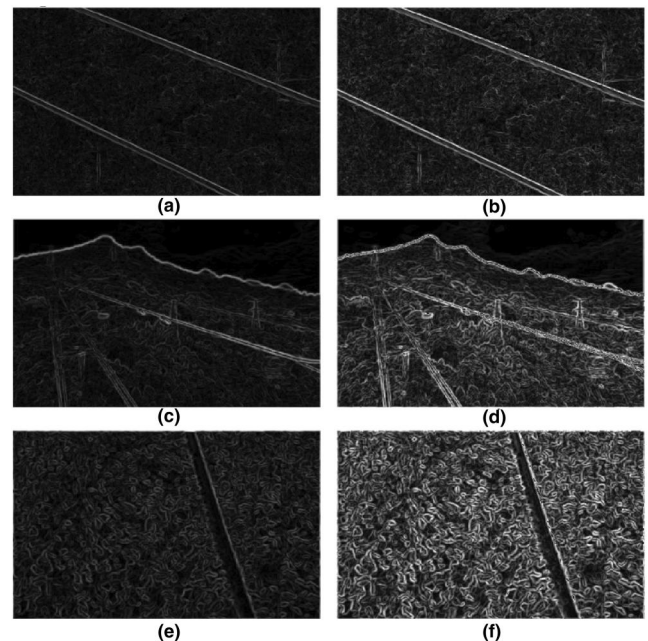


FIGURE 4 Convolution effect comparison of Sobel and Scharr operator (a), (c) and (e) are performed by Sobel operator, (b), (d) and (f) are performed by Scharr operator

### 3.2.2 | Line detection

The edge of the image includes conductor edges (namely valid edges) and background interference (namely invalid edges). Considering that the shape of HVTL in the image is often similar to straight lines, so the line detection of the Hough transform is chosen in this study to extract the conductor edges. The methods are as below:

An arbitrary straight-line in the  $x$ - $y$  coordinate system can be expressed in formula (3) and transpose it to get formula (4). Then a point  $(x, y)$  in the original  $x$ - $y$  coordinate system represents a straight-line in the  $k$ - $b$  coordinate system. Furthermore, a straight-line determined by two points represents an intersection in the new coordinate system. There are several points on this straight-line, which correspond to several straight-lines intersecting at one point in the  $k$ - $b$  coordinate system. In other words, the more straight-lines intersect at a point in the  $k$ - $b$  coordinate system, the higher probability that there is a straight-line in the  $x$ - $y$  coordinate system. In order to avoid slope  $k$  being equal to infinite, formula (4) is transformed into the polar coordinate to obtain formula (5).

$$y = kx + b \quad (3)$$

$$b = -kx + y \quad (4)$$

$$\rho = x \cos \theta + y \sin \theta \quad (5)$$

Next, count the number of straight-lines intersecting at a point in the  $\theta$ - $\rho$  coordinate system, and it is corresponding to that of the points on a line in the  $x$ - $y$  coordinate system. At the same time, a threshold is set through the complexity of the image background. Only when the number is higher than the threshold, the line composed of these edge points is considered as a straight-line segment. Otherwise, these edge points are deleted. And find all of the straight-line segments in the image by this way. Generally speaking, the conductor edge is a set of a series of long straight-line segments with similar slopes. However, the slope and length amplitude of the background interference line is random. Therefore, by counting the number of straight-line segments with the same slope and combining the length to realise dual constraints, the background interference can be filtered, and the pure straight-line segments at the edge of the conductor can be obtained.

### 3.2.3 | Straight-line segments clustering

Every conductor has two edges, and there may be multiple conductors on an image. Therefore, the belonging of the straight-line segments of the conductor edge obtained by the above method is undetermined. In other words, it is inevitable to determine further which conductor these edges belong. Unfortunately, the features of straight-line segments are not intuitive, and it is challenging to set labels to classify them directly. But the number of conductors is known, so their attribution can be determined by the clustering method.

K-Means clustering algorithm [31] has the advantages of simplicity, high efficiency, and good performance. It is mainly used to process point set and demanding only two parameters for each element in the set. However, for one straight-line segment, at least a pair of points, namely four parameters, are required to represent its characteristics. Besides, K-Means is suitable for processing points distributed in masses or clusters, and it is not effective when points are distributed linearly.

Consider the above shortcomings, an improved K-Means clustering algorithm based on a dynamic slope is proposed. The traditional K-Means algorithm uses distance as the criterion to calculate the distance from each point to the reference point (centroid) to determine the belonging of each point. Therefore, set a reference line in the image, calculate the distance from each straight-line segment to the reference line, and determine which edge it belongs to, based on the distance. However, the slope of each straight-line segment is different, and it is not parallel to the reference line; the distance between them cannot be calculated. So, the dynamic slope method is introduced. Set a reference point in the image, and use the slope of each straight-line segment as the slope of the reference line to calculate the distance from the reference line to the corresponding straight-line segment. Since the slope of the reference line varies with different straight-line segments, it is called a dynamic slope. A straight-line segment can be determined by the slope and the distance to the corresponding reference line, thereby reducing the four parameters that characterise the straight-line segment to two. On this basis, the K-Means clustering algorithm is used to solve the belonging of each straight-line segment. The steps of the algorithm are as follows:

- (i) Record the slope and intercept of  $n$  straight-line segments as  $k_1, k_2, \dots, k_n$  and  $b_1, b_2, \dots, b_n$ , respectively, and the number of clusters is twice the number of conductors, denoted as  $m$ .
- (ii) Set a reference point in the image, which can be selected arbitrarily in theory. Multiple experimental results show that the accuracy is higher if half of the image height is chosen as the  $x$ -coordinate value of reference point, so the reference point is set as  $(h/2, y_0)$ , where  $h$  and  $w$  are the height and width of the image, respectively, and  $0 < y_0 < w$ .
- (iii) Pass through the reference point  $(h/2, y_0)$ , and take  $k_1, k_2, \dots, k_n$  as the dynamic slope to draw the reference line, and calculate the distance  $d_i$  ( $i = 1, 2, \dots, n$ ) by formula (6).

$$d_i = \frac{\left| k_i \times \frac{h}{2} + (-1) \times y_0 + b_i \right|}{\sqrt{k_i^2 + (-1)^2}} \quad (6)$$

- (iv) Assuming that  $(d_i, k_i)$  represents the  $i$ th straight-line segment,  $(d_i, k_i)$  ( $i = 1, 2, \dots, n$ ) is substituted into the K-Means clustering algorithm, and they are divided into  $m$  classes. Till then, the tasks of dividing all straight-lines in the image have been completed.

Figure 5a and b is the results of clustering the straight-line segments of the conductor edge by using the traditional and dynamic slope K-Means algorithm, respectively. In Figure 5a, these points are distributed in four clustering regions after clustered, which cannot describe the shape of the conductors. However, the points distribution in Figure 5b shows an apparent linear trend, which can depict the trend of four edges of the two conductors. It is noticeable that the distribution of points in Figure 5a,b is different from the conductor trend in Figure 2a. That is due to the position of points in the image is indicated by the pixel coordinate system, namely, the  $U$ - $V$  coordinate system, where  $U$  and  $V$  represent the row and column that a point is located respectively and the origin of the  $U$ - $V$  coordinate system in the image is at the top-left corner, while the origin of the conventional  $X$ - $Y$  coordinate system is at the lower-left corner, which is equivalent to perform a coordinate transformation.

### 3.2.4 | Edge fitting

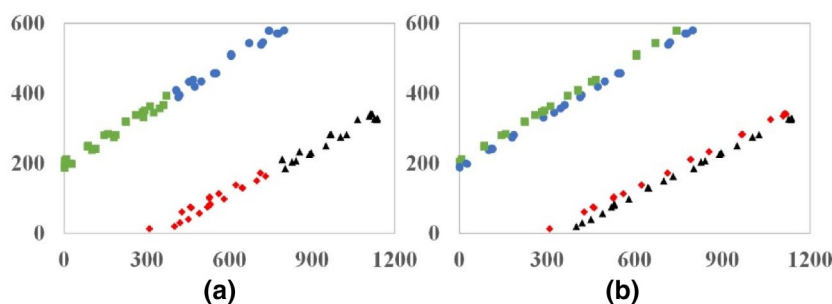
After determining the ownership of the straight-line segment of the conductor edge, the next step is to fit them as a complete edge. Since the slope of each straight-line segment is slightly different, the edges obtained by directly connecting them are not smooth. Therefore, the following steps are used:

- (i) Take the points at the beginning and end of each straight-line segment as feature points, denoted as  $[A_1(x_{A1}, y_{A1}), B_1(x_{B1}, y_{B1})], [A_2(x_{A2}, y_{A2}), B_2(x_{B2}, y_{B2})], \dots, [A_n(x_{An}, y_{An}), B_n(x_{Bn}, y_{Bn})]$ , where  $n$  is the number of straight-line segments of the conductor edge.
- (ii) According to formulas (7) and (8), the coordinate transformation is performed to obtain  $[A_1', B_1'], [A_2', B_2'], \dots, [A_n', B_n']$ , where  $h$  is the height of the image.

$$x' = |h - x| \quad (7)$$

$$y' = |y| \quad (8)$$

- (iii) Use the least-squares method [32] to fit the points after coordinate transformation to get the conductor edge in the  $X$ - $Y$  coordinate system.



(iv) Perform coordinate inverse transformation and draw the conductor edge in the  $U$ - $V$  coordinate system of the image. Finally, the black straight-lines that closely fit the two sides of the conductors in Figure 5c are the fitting results, which accurately locate the conductor edges.

## 4 | DISTANCE MAPPING AND THICKNESS CALCULATION

Once the conductor edge is located, taking any point on one edge of a single conductor, and calculating the distance from it to another edge of this conductor, which is the pixel width of the conductor, was carried out. However, the actual width of the conductor needs to be analysed comprehensively combined with the physical model. Generally speaking, the conversion between pixel distance and actual distance can be realised by the linear mapping method and the imaging formula combined with the similar triangle method [33]. In fact, the mapping relationship between the two is closer to nonlinearity, so this method has some errors. Qu et al. [33] proposed a stereo ranging model based on monocular vision (as shown in Figure 6), through which the distance from the optical centre of the camera to the measured point can be calculated. This model is improved to map the distance between any two points in the same plane to the actual distance in real coordinates, and realises the actual width of the conductor (as shown in Figure 7).

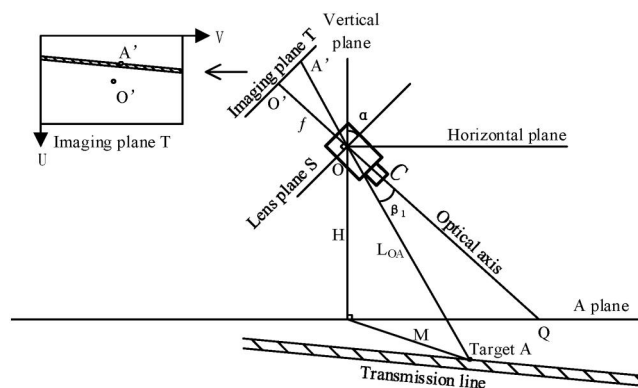


**FIGURE 6** Monocular vision ranging stereo model

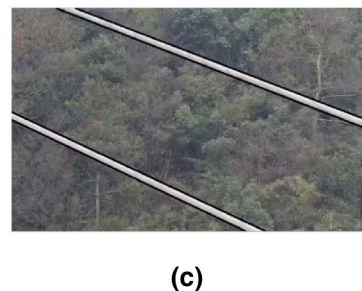


**FIGURE 5** Results of conductor feature points clustering and transmission line location (a) Traditional K-Means clustering, (b) Improved K-Means clustering, (c) Transmission line conductor location





8f are the edge location results of Figs. 8a, 8c, and 8e, respectively, when the light source is over the simulated conductor. It is clear that the edge position determined by the edge location algorithm closely fits both sides of the conductor, and the effect is ideal. Next, the application effect of the algorithm under different directions light source was further tested. Figure 9a,9c and 9e are the location results of three different conductors under the light source from the left side, and Figure 9b, d, and f are the results under the light source from the right side. It is clear that the algorithm has a relatively ideal result for the conductor location. The black lines in Figure 9a, b, c, d, and f are all attached to both sides of the conductor, which means the proposed algorithm located the conductor accurately. Only in Figure 9e, the black

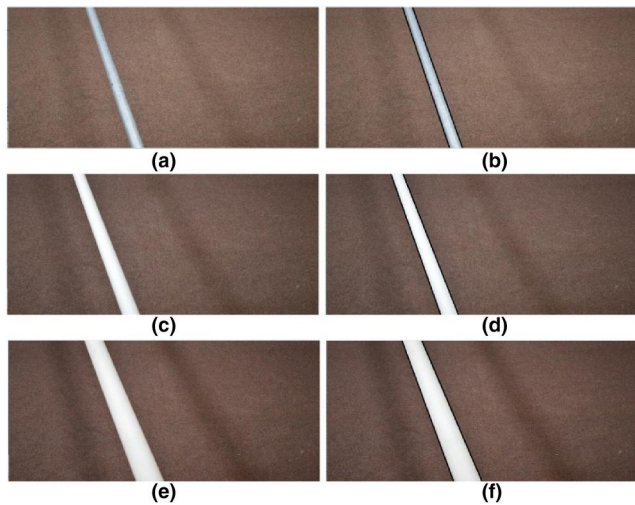


**FIGURE 8** Edge location results in experimental environment (a) Galvanised pipe, (b) Edge location of (a), (c) PVC pipe #1, (d) Edge location of (c), (e) PVC pipe #2, (f) Edge location of (e)

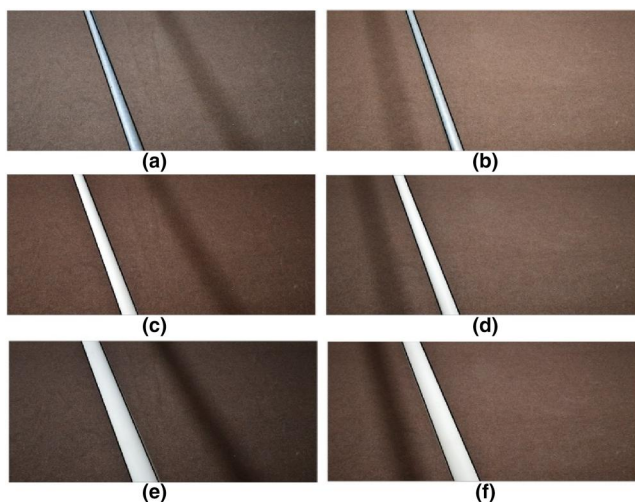


**FIGURE 9** Edge location under different light sources. (a) and (b) represent the effect of galvanised pipe under left and right light, (c) and (d) represent the effect of PVC pipe #1 under left and right light, (e) and (f) represent the effect of PVC pipe #2 under left and right light

line on the right side of the PVC pipe #2 under the light source on the left has a slight deviation to the actual conductor edge, but overall, it can still reflect the edge position of the conductor. In brief, it is believed that the effect of the proposed algorithm in the experimental environment meets the application requirements.

### 5.1.2 | Verification in field environment

Next, six images of the same HVTL under different illumination were obtained to test the algorithm further. The illumination changed from extremely weak to extremely strong in turn. The positioning effect is shown in Figure 10. Figure 10a was taken on a foggy day. The light intensity was extremely weak, and the trees and mountains in the background were covered by dense fog. Therefore, background interference is the least, and the effect of conductor location is the best. In Figure 10f, as the weather was clear and the light was extreme, the trees and mountains in the background were visible, which brought a lot of noise interference. So, the location effect is the worst. The location effect of the remaining images is between Figure 10a and f. Although the location effect of the algorithm on the conductor under different illumination is different, the black edge lines shown in Figure 10 can still locate the conductor edge accurately. In summary, it is believed that the proposed algorithm still shows strong location ability in complex field environments.

### 5.1.3 | Comparison

Wang et al. [35] used least-squares Hough transform (LSHT) to locate the conductor edge. The difference between the LSHT in [35] and the proposed method lies in the choice of the edge detection operator and the classification method of

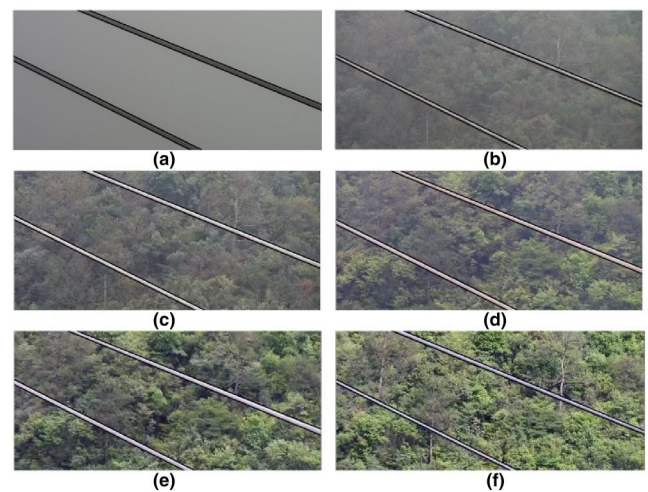


**FIGURE 10** Location results under different illumination (a) Weakest, (b) Weaker, (c) Weak, (d) Strong, (e) Stronger, (f) Strongest



the straight-line segments on the conductor edge. The former used the Sobel operator to convolve the image, but the choice of latter is the Scharr operator. More importantly, unlike the method used in this study to classify straight-line segments of the conductor edge using the improved K-Means algorithm, the LSHT in [35] first takes the points at the beginning and end of the straight-line segment as the feature points. Then, the least-squares method is applied to all feature points to determine the centreline when determining the belonging of the edge line segments. After that, the feature points are divided into two categories according to their distribution on the left or right side of the centreline. Finally, the two categories of feature points are respectively fitted, so as to locate the edges on both sides of the conductor.

Figure 11a and b is the results of processing the same image by the LSHT in [35] and the proposed method. It can be seen that the location result of the former is of deviation, while the result of the proposed method is accurate. In order to visualise the reason for the deviation of the LSHT, the straight-line segments of the conductor edge were extracted by the method in section 3.2.2. Then, the points at the beginning and end of the partial straight-line segment were adopted as the feature points to draw the scatter distribution map (as shown in Figure 12), where the straight line in the figure is the centre line fitted by feature points. It is easy to see that the feature points 6 and 7 in Figure 12 are all distributed on the centre line, and it is difficult to judge their belonging by the LSHT in [35], resulting in the two feature points being divided into the wrong edge. Further analysis of the reason is that the side of the



**FIGURE 11** Location results of different algorithms (a) LSHT, (b) Proposed method

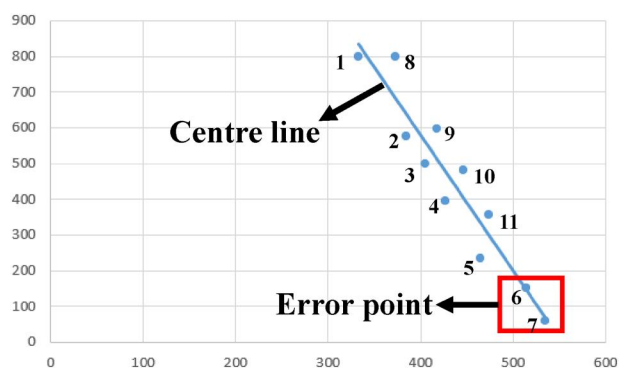


**FIGURE 12** Scatter diagram and centre line of feature points distribution of LSHT

conductor away from the camera is narrow, and the feature points there are closely arranged so that the fitted centreline may pass through some feature points. Transmission line images often show that the conductors extend far away, and the distal conductors are narrow. Therefore, the defects of the LSHT will affect accuracy. These two methods respectively processed 165 images, and the result is illustrated in Figure 13. The LSHT in [35] only accurately locates 77 images with an error rate of 53.33%. However, the proposed method accurately located 149 images with an error rate of only 9.70%. In other words, the proposed method is superior in the performance of conductor location, which is due to automatically adjust the slope of the reference line according to different straight-line segments and makes correct judgements on the attribution of each straight-line segment.

Furthermore, when there are multiple conductors in the image, LSHT in [35] will show more defects. Specifically, if the number of conductors is even (take 2 as an example), it is needed to use the least-squares method to fit the centreline firstly, where two conductors are distributed on both sides of the centreline. Then determining which conductor the feature points belong to base on their distribution on the left or right side of the centreline. After that, centrelines are fitted at each of the two conductors to determine whether the feature points come from the left edge or the right edge. Therefore, in the case of two conductors, the least-squares method is performed three times to determine the belonging of all feature points. Finally, it is necessary to continue to execute the least-squares method four times to fit the four edges of the two conductors. Overall, if the number of conductors is 2, the execution times of the algorithm are seven; if the number of conductors is 4, the times are as high as 15, which seriously affects the operational efficiency of the algorithm. To make matters worse, if the number of conductors is odd greater than one, the fitted centreline cannot be used to separate the conductors because the conductors on the image are generally not arranged at equal intervals. At this time, the LSHT in [35] can no longer even classify feature points. Since the bundle conductors are widely used in power systems, this defect will significantly limit the application of LSHT.

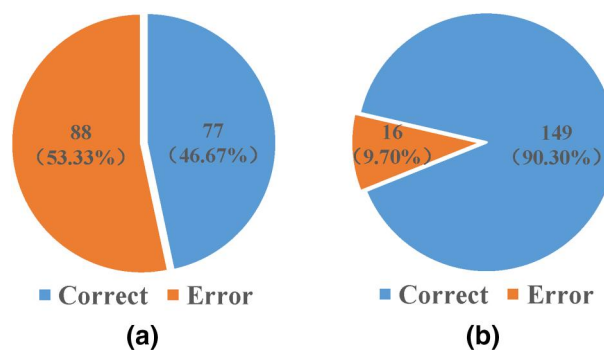


**FIGURE 13** Location accuracy between LSHT and proposed method (a) LSHT, (b) Proposed method

Compared with the LSHT in [35], the proposed method determines the belonging of the straight-line segments at the conductor edge through the K-Means clustering based on dynamic slope firstly and then fitting the edge. No matter the number of the conductor is odd or even, they can be classified accurately. The execution time of the algorithm is only twice the number of the conductor, which is obviously more efficient than LSHT. Simultaneously, multiple experimental results show that the improved K-Means algorithm spends about 0.08s to classify the straight-line segments once, and the performance time for the least square method once is about 0.03s. The more times of fitting, the lower the efficiency is. When the number of conductors is two or more, the processing speed of the proposed method is faster than LSHT. At present, the number of the bundle conductors of HVTL is generally between two and 4. It can be concluded that the applicability of the proposed method is stronger.

In summary, the proposed conductor location algorithm is superior to the LSHT in [35] in terms of accuracy, application range, efficiency, etc. And it can still work effectively when the number of conductors is odd; the overall performance is better.

## 5.2 | Verification of distance mapping model

### 5.2.1 | Performance analysis and comparison

In order to verify the accuracy of the distance mapping model based on the monocular vision in converting pixel distance to actual distance, the following experiment was designed. Through the calibration cloths located in outdoor and indoor environments in Figure 14, the distance between adjacent corner points on the calibration cloths in the two environments was calculated respectively to determine whether the results of calculation were affected by different environments. The parameters, including the height difference between the lens and the ground, the top-view angle of the lens, the distance between the lens and the calibration cloth in different scenes, were placed in Table 1. The size of the black square on the calibration cloth is  $20 \times 20$  cm.

In order to ensure that the corner points on the calibration cloth were located accurately, the Harris corner detection algorithm [36] was adopted to determine the internal corner

points with a size of  $6 \times 4$ . The yellow rectangle in Figure 15 is the detected corner points. The image in the rectangular frame is partially enlarged to clearly display the corner points (as shown in the lower part of the image in Figure 15a and b). Then the coordinates of corner points and environmental parameters were substituted into the distance mapping model to calculate 38 sets of adjacent corner spacing data in each image, and calculating the error between these data and the 20 cm standard value. The error distribution is shown in Table 2. It could be clearly seen from Table 2 that in outdoor and indoor environments, the scores with an error of less than 2.5% accounted for 78.95% and 81.58%, and the one less than 5% accounted for 86.84% and 92.11%, respectively. Through the above experiments, it can be considered that the proposed method can measure the actual distance between two points in the image accurately.

It is a traditional distance and linear mapping method to transform distance by applying the geometric relationship between image distance and focal length combined with similar triangles. For example, Wang et al. [35] introduced the formula of  $D = (v \cdot f) \times d / f$  to solve the actual width of the conductor, where  $D$  is the actual width of the conductor,  $v$  is the image distance,  $f$  is the focal length, and  $d$  is the projection width of the conductor in

TABLE 1 Environmental parameters

Scenes	Height difference, m	Top-view Angle, °	Distance, m
Outdoor	1.862	12	7–8
Indoor	1.318	10	6–7

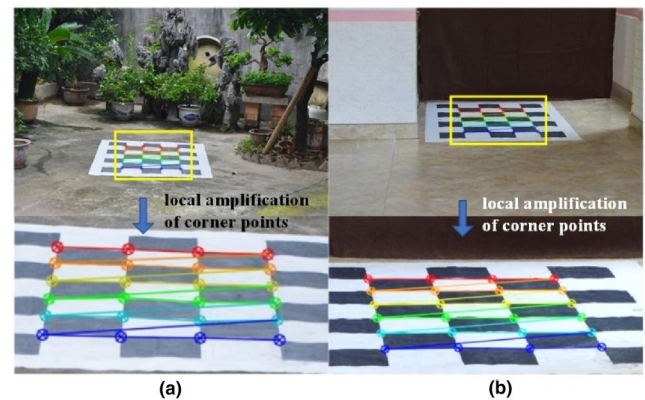


FIGURE 15 Detection result of corner points (a) Outdoor, (b) Indoor

TABLE 2 Error of calculating adjacent corner spacing

Scenes	Item	Error			Total
		<2.5%	2.5–5%	>5%	
Outdoor	Quantity	30	3	5	38
	Proportion	78.95%	7.90%	13.16%	100%
Indoor	Quantity	31	4	3	38
	Proportion	81.58%	10.53%	7.90%	100%



FIGURE 14 Performance of distance mapping model in different scenes (a) Outdoor, (b) Indoor

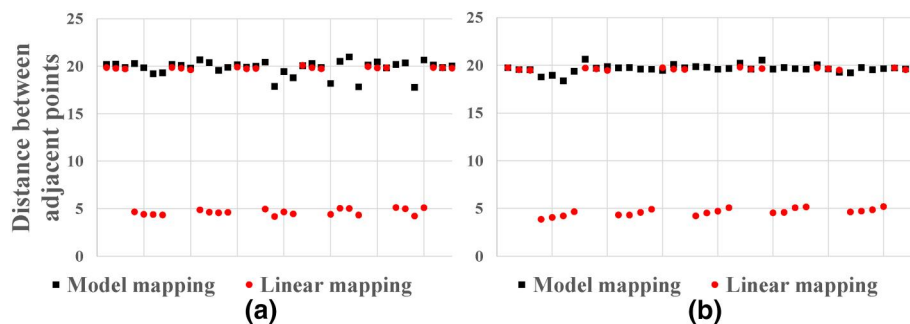


FIGURE 16 Calculation results of point spacing by different methods in different scenes (a) Outdoor, (b) Indoor

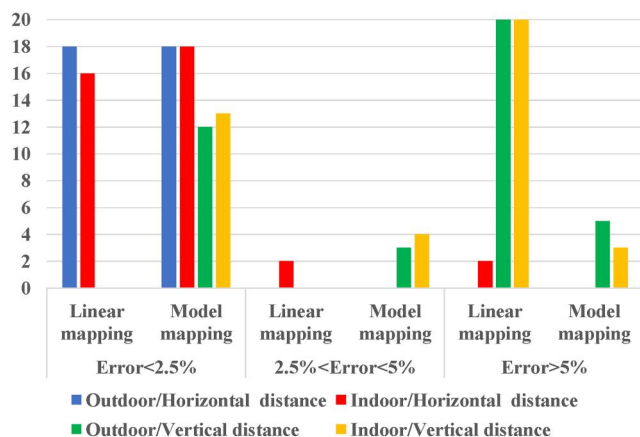


FIGURE 17 Comparison results at horizontal and vertical positions

the image. The distribution results of calculating the corner point spacing using the linear mapping method in [35] and the model mapping method proposed in this study in outdoor and indoor scenes are depicted in Figure 16a and b, respectively. The black dots in the figure are the calculation results using the model mapping method, and the red dots represented that of the linear mapping method. It can be found that, regardless of the indoor or outdoor environment, most of the calculation results of the model mapping method are close to the 20 cm standard value, and only a few have slight deviations. However, with the linear mapping method, only half of the calculated value of the points spacing approached the standard value, and the rest were deviated.

To further analyse the reasons for the deviation in the calculation results of the linear mapping method, the results were divided into two groups, horizontal and vertical. The statistical results are shown in Figure 17. In Figure 17, the blue and red bars representing the horizontal point spacing are mostly distributed within the error range of less than 2.5%, indicating that both methods can calculate the horizontal point spacing well. But for the green and yellow bars representing the vertical point spacing, all bars of the linear mapping method are located in the area where the error is greater than 5%. The calculating results of these point spacing deviated from the standard value, indicating that the linear mapping method

cannot be used to measure the vertical point spacing. Furthermore, most of the yellow and green bars of the model mapping method have an error of less than 2.5%, and only a small part is distributed in other areas, indicating the good results of the experiment. According to the experimental results, it is believed that the linear mapping method can calculate the horizontal points accurately, but has the defect in calculating the vertical point spacing. However, the model mapping method has excellent performance no matter in calculating the horizontal or vertical point spacing. That is, the model mapping method has better performance when converting the pixel distance to the actual distance.

### 5.2.2 | Anti-distortion ability analysis and comparison

In fact, for a uniform long object in the image, its pixel width is larger at the place near the lens and smaller at the distant place, but the actual width does not change with the distance from the lens. In order to test the anti-distortion ability of the mapping model, the following experiment was designed: take a piece of cloth with a width of 75 cm and a length that can exceed the shooting range of the lens, place red marks every 50 cm, as shown in Figure 18, and calculate the distance between adjacent marks.

The performance of the linear mapping methods of [20, 35] as well as proposed model mapping methods in recognition of horizontal and vertical spacing are shown in Table 3 and Table 4, respectively. In Table 3, the pixel width of the point pair A1-B1 closer to the camera is 821, and the farther pair A5-B5 is 481. The pixel width of A1-B1 is about 1.7 times that of A5-B5, which produced noticeable distortion of "near the far smaller", but the actual distance between the two pairs of points is 75 cm. The model mapping method was used to calculate their spacing, and the results are 72.898 and 71.250 cm, respectively, with an error of less than 5%. Further analysing another three sets of point pairs A2-B2, A3-B3, and A4-B4 could lead to similar conclusions. It is verified that the proposed model has a strong ability for anti-horizontal-distortion.

Similarly, for the performance of the model mapping method in the vertical point spacing. In Table 4, the pixel width



of the nearest point pair A1-A2 to the camera is 276.02, and the farthest pair A4-A5 is 125.88. The pixel width of A1-A2 is about 2.2 times that of A4-A5. Like the horizontal point, the distortion of 'near the far smaller' appears, and is even more intense. The actual distances of these two pairs of points are calculated by the model mapping method to be 47.739 and 46.958 cm, respectively, and the corresponding errors are 4.522% and 6.084%. Using the same method to calculate the point pairs B1-B2 and B4-B5 on the other side of the cloth, the actual distance and error are 47.604 and 46.993 cm, 4.792% and 6.014%, respectively. The calculation results on both sides of the cloth are similar, indicating that the distance calculation of the mapping model is not affected by the position of the

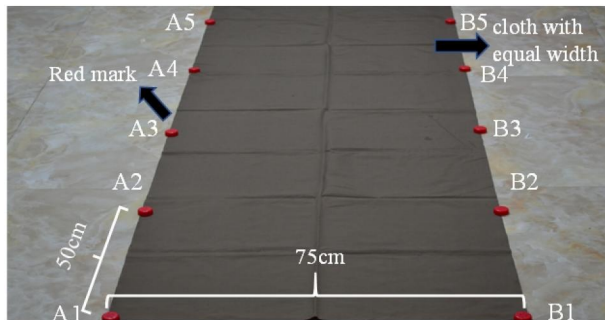


FIGURE 18 Anti-distortion ability test of ranging model

point pair in the image. Calculating the errors of the remaining point pairs, they are all less than 7.5%, and the average error is 5.331%. It can be considered that the proposed model has the ability of anti-vertical-distortion.

From Table 3 and 4, it can also be found that the average error of the horizontal point spacing calculated by the linear mapping method of [20] and that of [35] is 4.520% and 3.465%, respectively, indicating that it can deal with horizontal distortion. However, when calculating the vertical point spacing, the average error of [20] is 31.530% and that of [35] is as high as 56.139%, which proved once again that the method is not suitable to calculate the vertical point spacing. Overall, the model mapping method has a smaller average value of the horizontal point calculation error than the linear mapping method, and it has better performance. Moreover, its average vertical point calculation error is only 5.331%, much smaller than 31.530% and 56.139% of the linear mapping method. Therefore, the anti-distortion performance of the model mapping method is much better.

It should be noted that the distance between any two points in the image can be decomposed into horizontal and vertical distances. Therefore, distortion in either direction will affect the calculation results. The model mapping method has good ranging and anti-distortion performance in both horizontal and vertical directions. It can accurately calculate the distance between any pair of points in the same horizontal plane in the image.

TABLE 3 Anti-distortion performance test results in horizontal spacing

Mapping Method	Item	Target Point Pairs					Mean Value
		A1-B1	A2-B2	A3-B3	A4-B4	A5-B5	
---	Pixel width	821.00	707.00	615.04	540.00	481.00	
Linear mapping of [20]	Calculating value, cm	78.038	78.495	78.016	78.528	78.871	78.390
	Error, %	4.052	4.660	4.021	4.704	5.161	4.520
Linear mapping of [35]	Calculating value, cm	72.881	73.246	72.710	71.954	71.215	72.401
	Error, %	2.825	2.339	3.053	4.061	5.047	3.465
Model mapping	Calculating value, cm	72.898	73.246	72.916	72.087	71.250	72.479
	Error, %	2.803	2.339	2.779	3.884	5.000	3.361

TABLE 4 Anti-distortion performance test results in vertical spacing

Mapping Method	Item	Target Point Pairs								Mean Value
		A1-A2	A2-A3	A3-A4	A4-A5	B1-B2	B2-B3	B3-B4	B4-B5	
---	Pixel width	276.02	200.59	161.40	125.88	269.62	205.14	154.93	122.25	
Linear mapping of [20]	Calculating value, cm	41.467	37.002	32.557	26.002	40.977	37.425	34.155	24.293	34.235
	Error, %	17.066	25.996	34.886	47.996	18.046	25.150	31.690	51.414	31.530
Linear mapping of [35]	Calculating value, cm	28.596	20.782	21.506	18.772	23.886	24.376	18.410	19.116	21.931
	Error, %	42.808	58.436	56.988	62.456	52.228	51.248	63.180	61.768	56.139
Model mapping	Calculating value, cm	47.739	46.352	47.652	46.958	47.604	48.267	47.110	46.993	47.334
	Error, %	4.522	7.296	4.696	6.084	4.792	3.466	5.78	6.014	5.331

### 5.3 | Experimental environment setup

In order to verify the ability of the proposed method in identifying the ice thickness of the conductors on HVTL, a simulated icing experiment of the conductors was carried out in an experimental environment. The experimental environment is shown in Figure 19. The galvanised pipe with shape, colour, and size most similar to the aluminium conductor steel reinforced was selected for simulation (the diameter of the bundle conductor in 220kV HVTL is 2.25 cm, and the diameter of the galvanised pipe is 2.5 cm). The image was captured by a camera. Considering that the resolution of the field camera used is not high, the image taken in the experiment was compressed to 1280×720 resolution (i.e. One million pixels) as the original image. The height difference and the distance between camera and conductor, and the top-view angle of the camera were all measured by an infrared range and angle finder, the conductor width was measured by a vernier calliper, and the data was stored and processed by a portable computer. The iced conductor was made by inserting a galvanised pipe into a soft water pipe filled with water and putting it to the cold storage for freezing.

In order to verify whether the proposed algorithm can recognise the ice thickness of conductors in different environments, experiments were carried out under simple and complex backgrounds. The simple background was simulated by monochrome cloth and the complex background by camouflage cloth. Using a vernier calliper to measure the data three times at different positions of the conductor, and took the mean value as the thickness of the conductor. The average width of the un-iced conductor was 2.5 cm, and the average width of the iced conductor was 3.998 cm. So, the ice thickness was 1.498 cm. The height difference between the camera and the conductor was 112.25 cm, and the top-view angle of the camera was 32.27°.

### 5.4 | Performance of proposed method under various interferences

In fact, detecting the icing status of HVTL conductors in the field environment will be affected by various interference. The

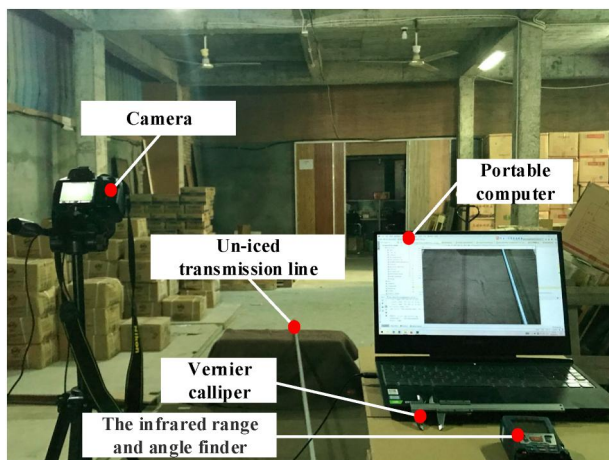


FIGURE 19 Experimental environment

analysis will be carried out by the following six aspects: different backgrounds, uneven icing, height difference changes, conductor movement, contrast changes, and conductor sag.

#### 5.4.1 | Different backgrounds

After obtaining the basic parameters required for calculation, five images of conductors with different slopes in the simple and complex background were respectively selected, and four of them are shown in Figure 20. Specially, all the 10 images were tested by the method of [20] and the proposed method, and the results are depicted in Figure 21. Obviously, no matter in the simple or complex background, the orange bars that representing the proposed method are closer to the standard value (2.5 cm) than the blue bars that stand for the method of [20]. Comparing the average calculation error of the two methods, the error of [20] is 11.96% and 14.30% in simple and complex backgrounds, respectively, while that of the proposed method is just 3.36% and 4.76%. It can be concluded that compared with

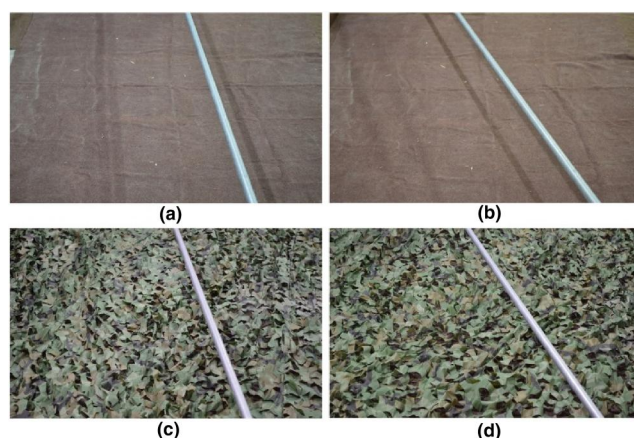


FIGURE 20 Conductors with different slopes in simple and complex background (a) and (b) are performed in simple background, (c) and (d) are performed in complex background

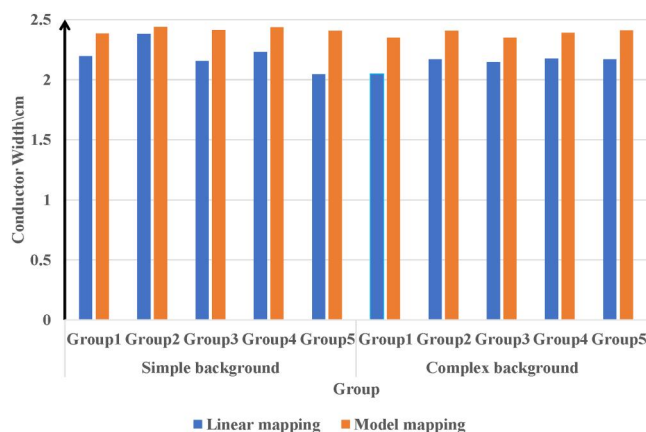
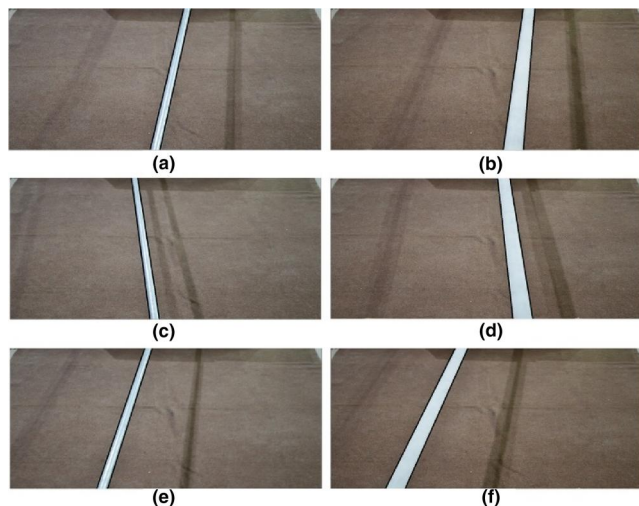


FIGURE 21 Recognition results of two methods



**FIGURE 22** Experiment under simple background. (a) Un-iced conductor in first group, (b) Iced conductor in first group, (c) Un-iced conductor in second group, (d) Iced conductor in second group, (e) Un-iced conductor in third group, (f) Iced conductor in third group

[20], the accuracy of the proposed method is improved by over 8%.

Besides, three groups of ice-covering thickness measurement experiments were carried out under the simple and complex background, and two test methods were used for processing. Method #1 was the method proposed in this study, and Method #2 was the LSHT combined with the linear mapping method in [35]. The experimental results of the proposed method under a simple background are depicted in Figure 22, where Figure 22a and b corresponds to the results before and after icing of the first group of experiments, Figure 22c and d correspond to the results of the second group, and Figure 22e and f correspond to the results of the third group. The experimental results of the proposed method under a complex background are depicted in Figure 23, and the image layout is consistent with Figure 22. It can be seen from Figures 22 and 23 that the proposed method can accurately locate the conductor before and after icing, regardless of the background is simple or complex.

The calculation results of ice thickness using Method #1 are shown in Figure 24a. The identification result for the iced conductor is close to the regular hexagon where the 4 cm scale is located, and the identification result for the un-iced conductor is close to the regular hexagon where the 2.5 cm scale is located. In other words, they are very consistent with the actual value of 3.998 cm for the iced conductor and 2.500 cm for the un-iced conductor. The experimental results of Method #2 are depicted in Figure 24b. It is clear that the identification result of Method #2 presented an irregular pattern. The calculated width of the conductor before and after icing has obvious deviation compared to the actual value, and some of the differences are larger. It should be noted that it is effective and meaningful to calculate the ice thickness if the conductor width was calculated correctly. Due to the large error in the identification result of Method #2,

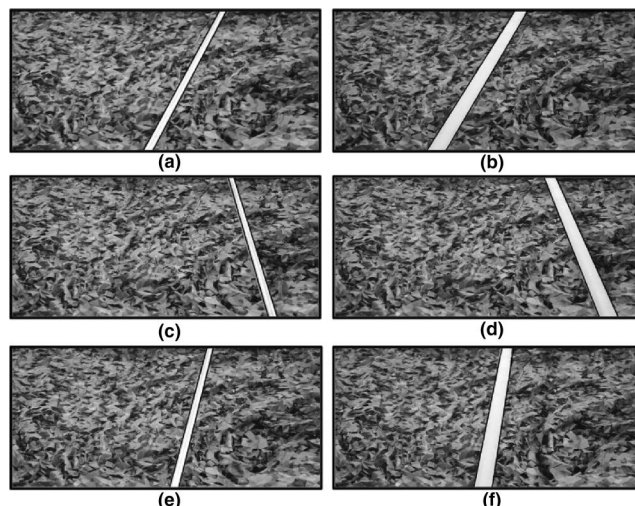


**FIGURE 23** Experiment under complex background (a) Un-iced conductor in first group, (b) Iced conductor in first group, (c) Un-iced conductor in second group, (d) Iced conductor in second group, (e) Un-iced conductor in third group, (f) Iced conductor in third group

the calculated ice thickness has no reference value. Therefore, only the performance of the proposed method in identifying ice thickness was tested. The results are shown in Table 5. The data in Table 5 shows that the calculated ice thickness approached the actual value of 1.498 cm. The recognition effect is better in a simple background, and the maximum error is less than 0.25 cm. In a complex background, some conductor features are easily lost due to background interference, and the accuracy of the algorithm is slightly decreased, but the error is still within 0.35 cm. In summary, the experiments show that the proposed method can be used to identify the ice thickness on transmission lines, and the effect is excellent.

#### 5.4.2 | Uneven ice

In some harsh environments, such as temperature between  $-3^{\circ}\text{C}$  and  $+2^{\circ}\text{C}$ , ice on the conductor will become extremely uneven and the glaze will appear [37, 38]. For this reason, a glaze on conductor was simulated in this study, which is shown in Figure 25. Due to the icicle on the surface, the edge of the iced conductor is no longer smooth and even. The width of the conductor with icicle was approximately 4.8–6.4 cm measured by a vernier calliper, which was significantly larger than the conductor with even ice. Considering that the ice thickness of the uneven-iced conductor is different in various parts, thus, the mean value of the ice thickness of the entire conductor is chosen to indicate the icing status.

The results of edge location and iced conductor width calculation are shown in Figure 26 and Figure 27, respectively. In Figure 26, the black line which depicts the edge of the conductor will no longer fit the ice layer of the cylinder, but located where the icicles are. However, it can also be observed from Figure 27 that the ends of some icicles are cone-shaped



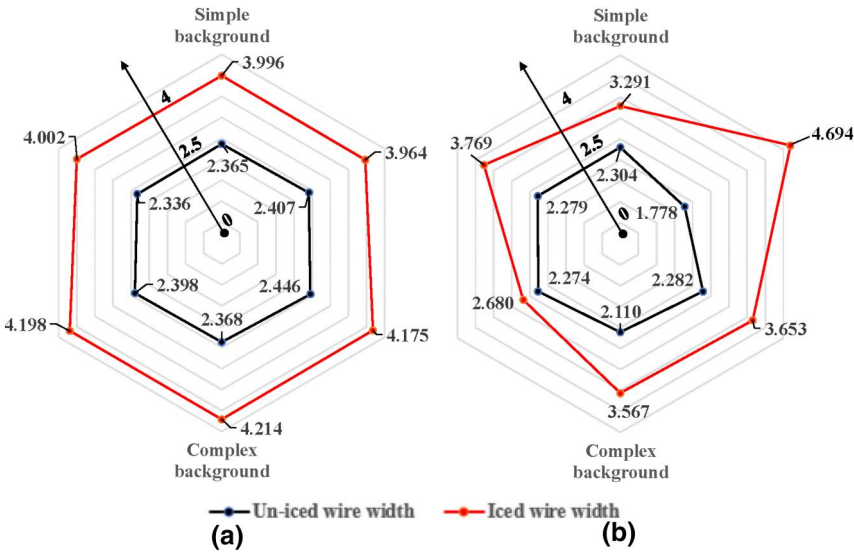


FIGURE 24 Recognition results of two methods (a) Method #1, (b) Method #2

TABLE 5 Three groups of recognition results in different backgrounds

Item	Simple Background			Complex Background		
	Group 1	Group 2	Group 3	Group 1	Group 2	Group 3
Width before icing, cm	2.365	2.407	2.446	2.368	2.398	2.336
Width after icing, cm	3.996	3.964	4.175	4.214	4.198	4.002
Calculated ice thickness, cm	1.631	1.557	1.729	1.846	1.800	1.666
Error, cm	0.133	0.059	0.231	0.348	0.302	0.168

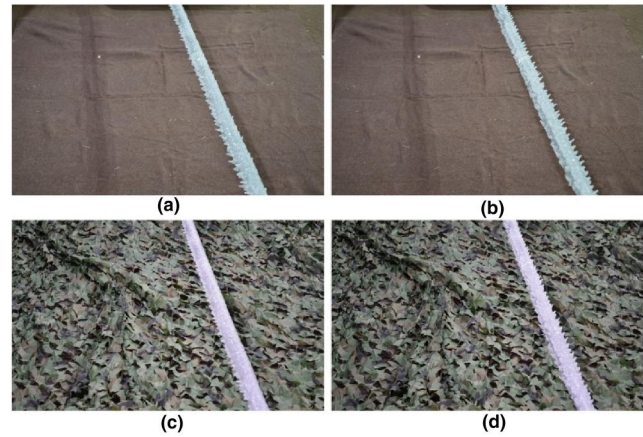


FIGURE 25 Uneven-iced conductors in different backgrounds (a) and (b) are performed in simple background, (c) and (d) are performed in complex background

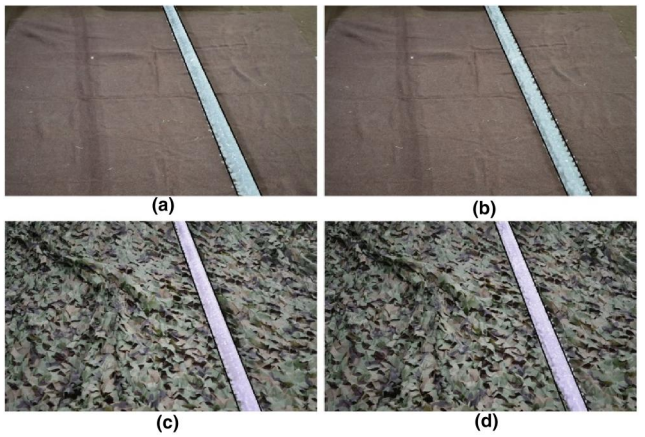


FIGURE 26 Location result of uneven-iced conductors (a) and (b) are performed in simple background, (c) and (d) are performed in complex background

with weak features. They are mixed with the background and ignored by the proposed method, which makes the conductor smaller for the calculated width compared to the actual width. Moreover, this phenomenon is more obvious in a complex background. But from the overall point of view, the proposed method can locate the iced conductor according to the position of the icicle which proves its ability to identify the uneven-

iced conductors. It can be illustrated from Figure 27 that the width of the iced conductor calculated by the proposed method is roughly between 5.2 and 6.1 cm, which is within the range of the actual width of 4.8–6.4 cm. Hence, the experimental results show the validity and reasonability of the proposed method. In summary, the proposed method can process uneven-iced conductors and accurately calculate their width.

### 5.4.3 | Height difference changes

If the height difference between the camera lens and the conductor is changed by the ice or wind, the conductor width obtained by the distance mapping model will deviate. To quantitatively analyse the influence of the height difference, the widths of the conductors at different height differences were tested in different states, and the results are shown in Figure 28. It can be seen that the conductor width varies with the height difference. The curve in Figure 28 is the result of fitting the width

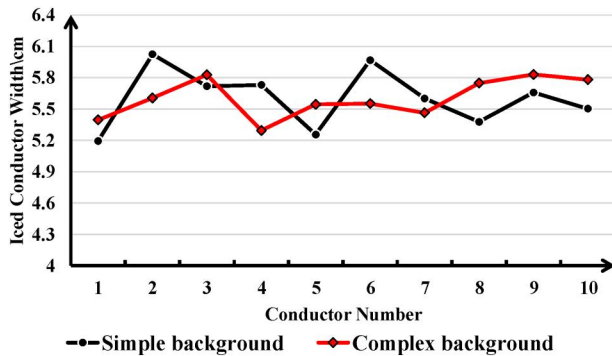


FIGURE 27 Recognition results of uneven-iced conductors in different backgrounds

of conductors at different heights, and it approaches a cubic function. What's more, if the height difference is within  $\pm 10$  cm (as the red dotted rectangle in Figure 28), the result is of a small deviation to the actual width of the conductor. Unfortunately, if the height difference is beyond this range, the accuracy of the algorithm decreases. In other words, the proposed method should be used in a certain scope in practical application. For example, the conductor with one end fixed on the hanging clamp can be chosen as the target due to its better tensile capacity and higher stability. Because the change of the conductor height difference at that position is the smallest within a span length when the environment changes, which is generally no more than 10 cm. In general, the status of the entire conductor within a span length is alike during icing. In this case, the proposed method can be guaranteed for better accuracy.

### 5.4.4 | Conductor movement

Conductor moving is related to the way of suspension and wind and generally occurs in the vertical plane [39]. It may have a height difference, and the influence of height difference on the algorithm has been detailed in Section 5.4.3. In addition, different wind speeds will result in various conductor vibration frequency, and the effect of photography is also different. This study will verify the influence of conductor vibration frequency on identification effect through experiments.

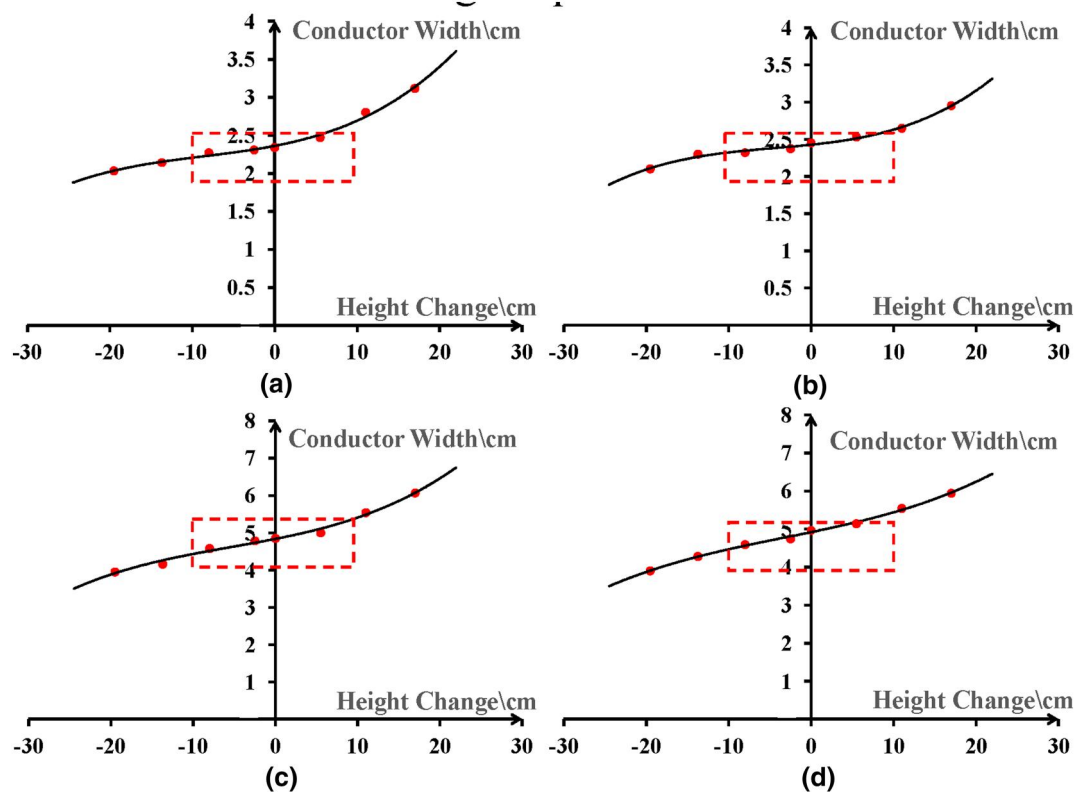
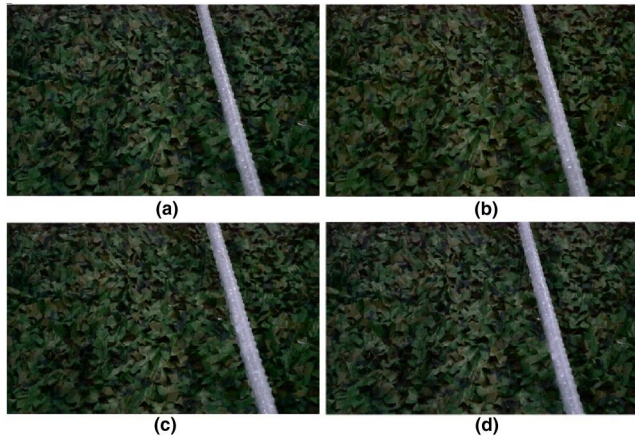


FIGURE 28 Influence of height difference changing on conductor width under different conditions. (a) Uniced conductor in simple background, (b) Uniced conductor in complex background, (c) Iced conductor in simple background, (d) Iced conductor in complex background



**FIGURE 29** Different positions of the conductors. (a) Position 1, (b) Position 2, (c) Position 3, (d) Position 4

In theory, there are three main types of conductor movements, in which the vibration frequency of conductor galloping and subspan oscillation is both below 5 Hz, which is less than the sampling frame rate of the camera (25fps). In the experiment, only the movement of the conductor in the vertical direction was simulated, then the movement of a conductor was recorded by video, and 25 frames of it were randomly intercepted. In Figure 29, four images of the conductor at different positions are shown as examples. It can be found that the clearness of the image is slightly reduced due to the movement of the conductor, but the conductor in it is still of sharp features. The proposed method can accurately locate all the images. However, the frequency of the aeolian vibration of the transmission line may be beyond 25 Hz, which will exceed the frame rate of the selected camera, and result in blurring or ghosting of the image. At this time, the diagnostic error of the algorithm will increase, or even leads to a failed localisation. In other words, as long as a clear image can be obtained, the proposed method can perform accurate location and identification. In extreme cases, the quality of images can be improved by using a high-performance camera.

#### 5.4.5 | Contrast changes

Contrast changes the difference between the foreground and background of the image. In order to test its influence on the proposed method, within the range of  $-90$  to  $100$ , the contrast of one image was adjusted at intervals of  $10$ , and a total of  $20$  different images were acquired. In Figure 30, four images with the contrast of  $-90$ ,  $0$ ,  $50$ , and  $100$  respectively are illustrated. Especially, the even-iced conductors ( $3.998$  cm), uneven-iced conductors ( $4.8$ – $6.4$  cm), and uniced conductors ( $2.500$  cm) were tested in different backgrounds. Six groups of experiments were carried out in total and the results are shown in Figure 31.

It can be observed in Figure 31 that the conductor width of each group decreased with the contrast reduced in the range of

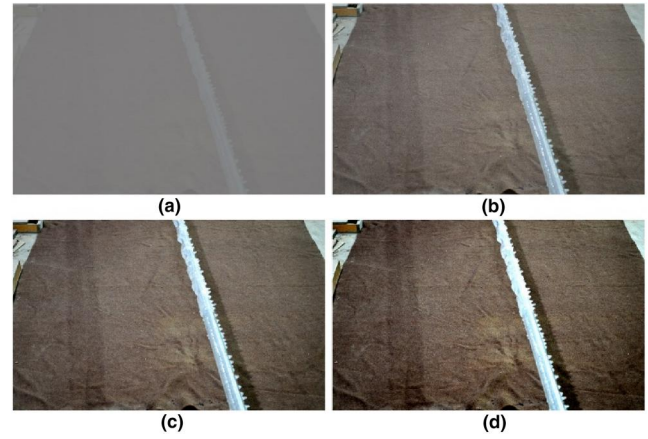


**FIGURE 30** Conductor image of different contrast (a)  $-90$ , (b)  $0$ , (c)  $+50$  (d)  $+100$

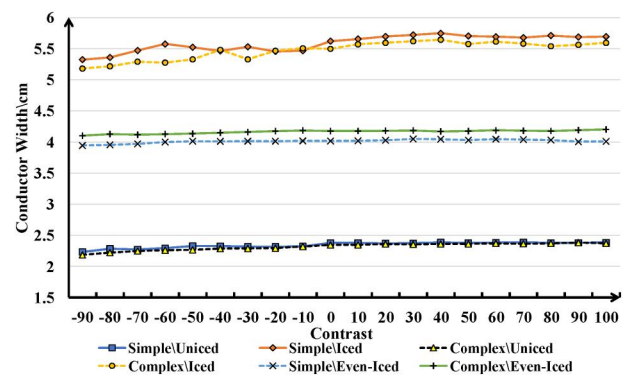


**FIGURE 31** Influence of contrast on conductors under different states

$-90$  to  $0$ . In particular, the deviation of uneven-iced conductors represented by the orange solid line and the yellow dashed line is larger than other curves. That is owing to the decrement of difference between the conductor and the background, which results in parts of the conductor edges mixed to the background. Especially, the uneven-iced conductor is particularly affected as the feature of the cone-shaped icicles on it are not prominent enough. Within the range of  $0$  to  $100$ , the curves show different trends. Among them, the orange and yellow curves tend to fluctuate after rising while the others remain basically stable. Further analysis of the phenomenon, when the contrast increases, the difference between the conductor and the background increases. Meanwhile, the stronger difference enhances the edge characteristics and further improves the ability of the proposed method in recognising icicles. On the other hand, the uniced and even-iced conductors with a smooth surface have sufficiently significant edge features when the contrast is  $0$ , so the identification effect of them is not significantly affected by the rise of contrast.

However, the difference between the background and the conductor simultaneously enhanced with the increased contrast, which brought new interference and affected the



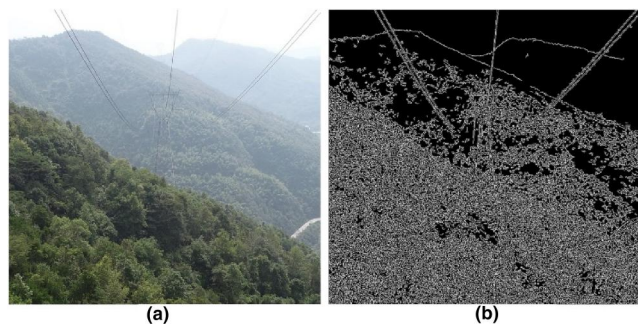


**FIGURE 32** Image of transmission line (a) Original image, (b) Image processed by improved Canny operator

accuracy of the proposed method. Therefore, the orange and yellow curves in Figure 31 fluctuates in the range of 0 to 100. It is noticeable in Figure 31 that if the contrast is less than  $-70$ , the error of the conductor width is the highest, but still within 10%. On the contrary, if it is between  $-70$  and 100, the error is less than 5 %, which proves the good performance of the proposed method when the contrast varies.

#### 5.4.6 | Conductor sag

In fact, HVTL all have sag due to gravity. As shown in Figure 32a, the shape of the transmission line within a span length is similar to a parabola, and the conductor is narrow. These factors will affect the accuracy of the proposed method. The edge of the image is extracted by the proposed improved Canny algorithm, which is illustrated in Figure 32b. There is no obvious difference between the edge feature of mountain and conductor, which makes them tough to be separated from each other. At the same time, the features of the conductor in the distance are weak and difficult to identify. What's worse, as shown in Figure 32a, the width of narrow conductors only takes up about two to three pixels in the image, which leads to an extreme sensitivity to the noise when calculating.

The solution to the above problem is to select the conductor near the suspension point as the detection target. Because the conductor near that position has the strongest tensile strength, the smallest sag, and the shape is the same as a straight-line. Moreover, the conductor of the selected position is closer to the camera so that the width of it in the image is wider, which is conducive to algorithm analysis. In summary, the sag of the conductor has a certain influence on the proposed method, but the influence can be weakened by selecting the conductor at a suitable position.

## 6 | CONCLUSIONS

In order to detect the icing status of the High-voltage transmission line (HVTL), a method based on dynamic slope K-Means clustering and distance mapping is introduced to identify the ice thickness of the HVTL in this

study. Compared with the existing methods, the proposed method is mainly improved and optimised in the following three aspects:

- (i) An ice thickness identification method based on pure machine vision is proposed. Compared with other methods requiring tension sensors or binocular cameras, this study just requires an ordinary camera to collect images. It has the advantage of easy installation and it is no need to change the structure of the transmission line which avoids a blackout when operating and maintaining. Moreover, it is easy to obtain the parameters required for calculation.
- (ii) A novel dynamic slope K-Means clustering algorithm is introduced to classify the straight-line segments of the transmission line edge. On this basis, the conductors in the image are located. The experiments show that the accuracy of location in different backgrounds is 90.30%.
- (iii) A mapping model based on monocular vision ranging is constructed. First, the distance between the lens of the camera and the measured point is calculated through the monocular vision ranging model so that the depth information of image is restored. After that, the pixel width of the conductors in the image is mapped to the actual width by the distance mapping model. The model has anti-distortion, ensuring the width of the transmission line can be accurately calculated regardless of the distance from the camera and the error is within 6%.

Meanwhile, the experimental results show that the proposed method has good anti-interference performance under the conditions of uneven icing, height difference changes, conductor movement, contrast changes, and conductor sag. Therefore, it has a good prospect in practical application.

For future work, the following three aspects will be focus on:

- (i) Improving the ability of algorithm in locating conductors under intense illumination.
- (ii) Enhancing the ability of distance mapping model to resist distortion, height difference changes and conductor movement.
- (iii) Collecting different types of iced conductor images and test the performance of the proposed method when facing various types of ice-coating and improving the algorithm further.

## ACKNOWLEDGEMENTS

This work was supported in part by the National Natural Science Foundation of China under Grant 51677030.

## REFERENCES

- Nazir, M.T., et al.: Laboratory investigation on hydrophobicity of new silicon rubber insulator under different environmental conditions. *Int. J. Electr. Comput. Sci.* 12, 1–8 (2012)
- Wang, W.J., et al.: Study on sustainable development of power transmission system under ice disaster based on a new security early warning model. *J. Clean Prod.* 228, 175–184 (2019)

3. Jiang, X., et al.: Predictive model for equivalent ice thickness load on overhead transmission lines based on measured insulator string deviations. *IEEE Trans. Power Deliv.* 29(4), 1659–1665 (2014)
4. Hu, J.L., et al.: DC flashover performance of various types of ice-covered insulator strings under low air pressure. *Energies*. 5, 1554–1576 (2012)
5. Hu, J.L., et al.: DC flashover performance of ice-covered composite insulators with parallel air gaps. *Energies*. 8(6), 4983–4999 (2015)
6. Hu, Y.Y., et al.: DC flashover performance of ice-covered insulators under complex ambient conditions. *IET Gener. Transm. Distrib.* 10(10), 2504–2511 (2016)
7. Shu, L.C., et al.: Three-dimensional electric field simulation and flashover path analysis of iced-covered suspension insulators. *High Volt.* 5(3), 327–333 (2020)
8. Yin, F.H., et al.: Electrical characteristics of an energized conductor under various weather conditions. *High Volt.* 2(2), 102–109 (2017)
9. Huang, X.B., et al.: An online monitoring technology of tower foundation deformation of transmission lines. *Struct. Health Monit.* 18(3), 949–962 (2019)
10. Cui, F.J., et al.: Study on the influence of interphase spacers on ice shedding of three-phase iced eight-bundled transmission lines. *Cold Reg. Sci. Tech.* 174, 1–14 (2020)
11. Jiang, X.L., et al.: Site experimental study on suspension-tension arrangement for preventing transmission lines from icing tripping. *Int. J. Electr. Power Energy Syst.* 119, 1–7 (2020)
12. Zhao, J.K., et al.: Icing monitoring system of transmission lines based on image and stress. In: 2nd IEEE Conf. on Energy Internet and Energy System Integration (EI2), Beijing, October(2018), pp. 1–4
13. Jiang, X.L., et al.: Predictive model for equivalent ice thickness load on overhead transmission lines based on measured insulator string deviations. *IEEE Trans. Power Deliv.* 29(4), 1659–1665 (2014)
14. Ma, G.M., et al.: The reusable load cell with protection applied for online monitoring of overhead transmission lines based on fibre bragg grating. *Sensors*. 16(6), 1–13 (2016)
15. Huang, X.B., et al.: An online technology for measuring icing shape on conductor based on vision and Force sensors. *IEEE Trans. Instrum. Meas.* 66(12), 3180–3189 (2017)
16. Yang, L., et al.: Recognition of natural ice types on in-service glass insulators based on texture feature descriptor. *IEEE Trans. Dielectr. Electr. Insul.* 24(1), 535–542 (2017)
17. Guo, Q.L., et al.: New key point matching method using local convolutional features for power transmission line icing monitoring. *Sensors*. 18(3), 1–15 (2018)
18. Guo Q.L., Hu X.G.: Power line icing monitoring method using binocular stereo vision, In: 12th IEEE Conf. on Industrial Electronics and Applications (ICIEA), Siem Reap, Cambodia, June 2017, pp. 1905–1908.
19. Ma, Y., et al.: Measurement of ice thickness based on binocular vision camera. In: IEEE Int. Conf. on Mechatronics and Automation (ICMA), Takamatsu, Japan, August, 2017, pp. 162–166
20. Li, J., et al.: The icing-thickness detection of high-voltage transmission line based on machine vision. In: IEEE Int. Conf. on Mechatronics and Automation (ICIA), Macau, China, July 2017, pp. 381–385
21. Akram, S., et al.: Dielectric properties and modelling of multilayer polyimide nanocomposite to highlight the impact of nanoparticles dispersion. *IEEE Trans. Dielectr. Electr. Insul.* 27(4), 1238–1246 (2020)
22. Han, Y., Chu, Z.N., Zhao, K.: Target positioning method in binocular vision manipulator control based on improved canny operator. *Multimed. Tools Appl.* 79(13–14), 9599–9614 (2020)
23. McIlhagga, W.: The canny edge detector revisited. *Int. J. Comput. Vis.* 91(3), 251–261 (2011)
24. Cao, X.H., et al.: Detection method for auto guide vehicle's walking deviation based on image thinning and Hough transform. *Meas. Control.* 52(3–4), 252–261 (2019)
25. Zhao, L., et al.: Automatic extraction algorithm of power line in complex background. *High Volt. Eng.* 45(1), 218–227 (2019)
26. Hao, Y.P., et al.: Wavelet image recognition of ice thickness on transmission lines. *High Volt. Eng.* 40(2), 368–373 (2014)
27. Tian, Y.T., et al.: A method for power system static stability situation assessment based on scale invariant feature transform. In: Int. Conf. on power System Technology (POWERCON), November, Guangzhou, China (2018), pp. 4124–4129
28. Ali, P., Homayoun, M.N.: A robust digital image watermarking scheme based on bat algorithm optimization and SURF detector in SWT domain. *Multimed. Tools Appl.* 79(29–30), 21653–21677 (2020)
29. Ma, C.Q., et al.: Improved ORB algorithm using three-patch method and local grey difference. *Sensors*. 20(4), 1–26 (2020)
30. Cao, J.F. et al.: Implementing a parallel image edge detection algorithm based on the Otsu-canny operator on the hadoop platform. *Comput. Intell. Neurosci.* 1–13 (2018)
31. Khanmohammadi, S., et al.: An improved overlapping k-means clustering method for medical applications. *Expert Sys. Appl.* 67, 12–18 (2017)
32. Geng, P.B., et al.: Multipath least squares algorithm and analysis. *Signal Process.* 174, 107633 (2020)
33. Qu, S.S., et al.: A method for measuring the height and area based on distance estimation of monocular vision. *Sci. Tech. Eng.* 16(2), 224–228 (2016)
34. Yu, W.B., et al.: Research of improved Zhang's calibration method. In: 2017 Chinese Automation Congress (CAC), Jinan, China, October 2017, pp. 1423–1427
35. Wang, J.J., et al.: Image recognition of icing thickness on power transmission lines based on a least squares Hough transform. *Energies*. 10(4), 1–15 (2017)
36. Wang, D.Y., et al.: Combined use of FCN and Harris corner detection for counting wheat ears in field conditions. *IEEE Access*, 7, 178930–178941 (2019).
37. Farzaneh, M.: Atmospheric icing of power networks. Springer Netherlands, Berlin (2008)
38. Yin, F.H., et al.: Laboratory investigation of AC corona loss and corona onset voltage on a conductor under icing conditions. *IEEE Trans. Dielectr. Electr. Insul.* 23(3), 1862–1871 (2016)
39. Gurung, C.B., et al.: Identification of large amplitude wind-induced vibration of ice-accreted transmission lines based on field observed data. *Eng. Struc.* 24(2), 179–188 (2002)

**How to cite this article:** Weng, B., et al.: Newly designed identifying method for ice thickness on high-voltage transmission lines via machine vision. *High Volt.* 6(5), 904–922 (2021). <https://doi.org/10.1049/hve2.12086>